Identification of functional immune and neuronal tumour cells in glioma

Rachel Naomi Curry, B.A. [1,2], Malcolm F. McDonald, B.S. [3,4,+], Qianqian Ma, Ph.D. [5+], Jochen Meyer, Ph.D. [6], Isamu Aiba, Ph.D. [6], Brittney Lozzi [2], Alexis Cervantes [2], Yeunjung Ko, M.S. [2], Estefania Luna-Figueroa [2], Dong-Joo Choi, Ph.D. [2], Zhung-Fu Lee [2], Junzhan Jing, Ph.D. [2], Arif O. Harmanci, Ph.D. [7], Anna Rosenbaum [2], Peihao He [2], Carrie Mohila, M.D. Ph.D. [8], Ali Jalali, M.D. Ph.D. [9], Jeffrey Noebels, M.D., Ph.D. [5,6,11], Xiaolong Jiang, Ph.D. [5,10], Benjamin Deneen, Ph.D. [2,5,9,*,‡], Ganesh Rao, M.D. [5,9,*,‡], Akdes Serin Harmanci, Ph.D. [5,9,*, ‡]

[1] Graduate School of Biomedical Sciences, Baylor College of Medicine, Houston, TX

[2] Center for Cell and Gene Therapy, Baylor College of Medicine, Houston, TX

[3] Medical Scientist Training Program, Baylor College of Medicine, Houston, TX

[4] Development, Disease Models, and Therapeutics, Baylor College of Medicine, Houston, TX

[5] Center for Cancer Neuroscience, Baylor College of Medicine, Houston, TX

[6] Department of Neurology, Baylor College of Medicine, Houston, TX

[7] School of Biomedical Informatics, University of Texas Health Science Center, Houston, TX

[8] Department of Pathology, Texas Children's Hospital, Houston, TX

[9] Department of Neurosurgery, Baylor College of Medicine, Houston, TX

[10] Jan and Dan Duncan Neurological Research Institute, Texas Children’s Hospital, Houston, TX

[11] Department of Human and Molecular Genetics, Baylor College of Medicine, Houston, TX

[+] These authors contributed equally to this work

* These authors contributed equally to this work

[‡] Corresponding Author

Abstract

Despite advances in molecular profiling, therapeutic development has been hindered by the inability to identify and target tumour-specific mechanisms without consequence to healthy tissue. Correspondingly, a computational framework capable of accurately distinguishing tumour from non-tumour cells has yet to be developed and cell annotation algorithms are unable to assign integrated genomic and transcriptional profiles to single cells on a cell-by-cell basis. To address these barriers, we developed the Single Cell Rule Association Mining (SCRAM) tool that integrates RNA-inferred genomic alterations with co-occurring cell type signatures for individual cells. Applying SCRAM to glioma, we identified tumour cell trajectories recapitulate temporally-restricted developmental paradigms and feature unique co-occurring identities. Specifically, we validated two previously unreported tumour cell populations with immune and neuronal signatures as hallmarks of human glioma subtypes. *In vivo* modeling revealed a rare immune-like tumour cell population resembling antigen presenting cells can direct CD8+ T cell responses. In parallel, Patch sequencing studies in human tumours confirmed that neuronal-like glioma cells fire action potentials and represent 40% of *IDH1* mutant tumor cells. These studies identified new glioma cell types with functional properties similar to their non-tumour analogues and demonstrate the ability of SCRAM to identify these cell types in unprecedented detail.

Introduction

In the era of cancer genomics, the advent of high-throughput single cell sequencing technologies has allowed for examination of cellular heterogeneity in genomic, transcriptomic and epigenomic detail[1]. Studies employing these technologies have demonstrated dynamic cellular and subcellular hierarchies that are spatiotemporally distinct and have revealed transcriptional profiles that can be utilized to classify tumours into clinically-relevant molecular subtypes[2–5]. Despite these advances, the ability of sequencing pipelines to reliably identify tumour cells and the co-occurring genomic and transcriptomic cell states that define them has yet to be attained. Within malignant glioma, the most lethal form of brain tumors, resolution of this complexity represents a major impediment to therapeutic development that is further compounded by a diverse cellular constituency, complex array of tumour-specific genetic variants and inability to distinguish glioma cells from their non-tumor counterparts. To this end, we have developed a novel single cell computational tool, Single Cell Rule Association Mining (SCRAM) capable of accurately identifying tumour cells and defining co-occurring cellular states for individual cells. SCRAM integrates three orthogonal features to identify tumour cells in single cell resolution: (1) cell type transcriptional profiling; (2) RNA-inferred copy number variant (CNV) calling; and (3) RNA-inferred single nucleotide variant (SNV) calling. Our studies revealed that more than half of tumour cells feature transcriptional profiles matching more than one cell type, including an infrequent astrocytoma-specific population with transcriptional and functional properties of antigen presenting immune cells. In parallel, SCRAM uncovered that the majority of *IDH1* mutant ($IDH1^{mut}$) tumour cells possess GABAergic neuronal-like transcriptomes and fire action potentials. Our observations demonstrate that tumour cells endowed with immune and neuronal expression profiles can acquire functional cellular states and highlight the utility of using our computational framework for characterizing pseudo cell types in cancer.

Results

SCRAM reliably discriminates between tumour and non-tumour cell types

To validate SCRAM as a reliable computational framework (**Fig. 1A**), we examined whether SCRAM annotation was consistent with established transcriptional profiles for previously published human and mouse single-cell RNA-sequencing (scRNA-seq) datasets. We manually curated a cell type marker list for assigning cell identities based on at least two cell type–specific markers reported by EnrichR[6], Allen Brain Atlas[7,8], and other studies (**Fig. S1, Tables S1,2**). SCRAM could assign cell type identities to greater than 75% of cells across eight scRNA-seq datasets (**Fig. 1B**) and identified greater than 83% of cells as possessing transcriptional profiles meeting the criteria for multiple cell types (**Fig. 1C**). Using established glioma transcriptional profiles[5,9] and our manually curated marker list, we assigned cell type annotation to individual cells and found that SCRAM-assigned identities were consistent with those defined in previous reports (**Figs. 1D–G**). Our analysis found that greater than two-thirds of sequenced cells exhibited co-occurring cell type annotations, suggesting that glioma cells possess transcriptional signatures consistent with multiple cellular states. Further validation using the 10X Genomics spatial transcriptomics dataset of *IDH1*–wild-type ($IDH1^{WT}$) glioma revealed that various permutations of co-occurring cellular states exist within single-cell clusters, demonstrating that clusters encompass a heterogenous group of cell types with various genomic and transcriptomic profiles (**Figs. 1H,I; S2A**). Because SCRAM can define both transcriptional signatures and RNA-inferred genomic CNVs, we were able to further characterize the respective lineages of tumour cells. Our results confirmed that tumour cells are spatially dispersed throughout the non-tumour landscape and present with diverse transcriptomic cellular profiles within a small anatomical region. These analyses validated the ability of SCRAM to replicate previously defined cellular annotations and demonstrated the ability of SCRAM to resolve intra-tumoural heterogeneity by defining co-occurring cellular identities and cellular states with high resolution.

After confirming the capacity of SCRAM to accurately assign cellular identities, we assessed the ability of SCRAM to distinguish tumour cells from non-tumour cells. We analysed non-tumour human and mouse cortex scRNA-seq datasets from the Allen Brain Atlas and found that SCRAM reliably distinguished tumour from non-tumour cells with greater than 99% accuracy across species. SCRAM was able to annotate greater than 88% of cells in these datasets, replicating 60% and 86% of the Allen Brain Atlas annotations for the human and mouse datasets, respectively (**Figs. 1J,K; S2B,C**). Individual cellular annotations revealed that clusters comprised heterogeneous cell types, and we further refined these expression signatures using the *de novo* marker function in SCRAM (**Figs. S2D–G**). These data demonstrate that SCRAM reliably distinguishes between tumour and non-tumour cell types and accurately assigns cell identities in humans and mice. Furthermore, these studies highlighted the utility of SCRAM for examining single-cell expression profiles and characterizing cellular heterogeneity in the mammalian brain.

SCRAM elucidates novel developmental tumour cell states in glioma

Having validated SCRAM, we next aimed to define the genomic and transcriptomic landscape of tumour cells in our integrated scRNA-seq dataset consisting of 195,063 cells from seven malignant glioma patients (**Fig. S3A; Table S3**). SCRAM analyses employing the CaSpER[10] CNV-calling algorithm (**Figs. S3B,C**) confirmed that IDH1^{WT} tumours had increased CNV incidence (**Figs. 2A–D; S3D,E**), whereas chromosome 1p19q co-deletions were the predominant alterations in IDH1^{mut} oligodendroglioma. Parallel analyses using XCVATR[11] to call SNVs validated that IDH1^{mut} tumours featured *IDH1* mutations, whereas IDH1^{WT} tumours featured *EGFR*, *TP53,* and *PTEN* mutations (**Figs. 2E,F; S3F,G**). Although DNA-based sequencing studies have described a higher mutational burden in IDH1^{WT} tumours, our RNA-inferred analyses identified more frequent SNV transcription at the mRNA level in IDH1^{mut} glioma than in IDH1^{WT} glioma. Of particular interest was the high incidence of mutations in a

transcript mapping to the polycomb repressive complex 2 (PRC2) *SUZ12* sequence. Further examination revealed that the mutated *SUZ12* sequence is identical to the *SUZ12* pseudogene (*SUZ12P1*) sequence. This transcript was detected at high levels in all glioma patients, suggesting either that *SUZ12* mutations are the most transcribed SNVs in our cohort or that *SUZ12P1* is actively transcribed in glioma patients (**Figs. 2G,H; S3H**). Prior reports have observed hypermethylation of PRC2 regions in malignant tumours, which is pronounced in IDH1^{mut} subtypes[12,13] and has identified mutant *SUZ12* as a driver of some peripheral nervous system malignancies[14,15]. Whether high transcriptional penetrance of *SUZ12P1* or mutated *SUZ12* mechanistically contributes to malignant glioma warrants future mechanistic inquiries.

Using CNV and SNV annotation, together with established tumour marker expression (**Fig. 2I; Figs. S4A–F**), cells were assigned tumour or non-tumour status (**Fig. 2J**). Tumour cells in both IDH1^{WT} and IDH1^{mut} samples primarily mapped to one of three SCRAM-assigned cell classes (embryonic-neural, embryonic, or neural) and one of four co-occurring cell lineages (glial, glial-neuronal, myeloid, or neurodevelopmental), emphasizing shared transcriptomic features among glioma subtypes (**Figs. S5A–D**). An examination of cell types by patient revealed within- and between-patient heterogeneity and illuminated various myeloid-derived immune cell signatures within IDH1^{mut} tumour core samples (**Fig. 2K; S5A–D**). Importantly, CNVs were the only marker in 17% of tumour cells, representing a tumour cell population that could not be assigned to any cell type (**Fig. S5E**). Using the SCRAM *de novo* marker function, we identified markers of these unclassified tumour cells, which include *TRIO, RNF180* and *ELL2* for cells with chromosome 5 and 7 gains, and *STAU1, NAA20* and *DSTN* for cells with chromosome 20 gains (**Table S4**). Since *de novo* marker genes are differentially expressed in CNV-bearing tumor cells, they may serve as putative tumor-specific markers of glioma cells and should be further studied in future scientific endeavours. Collectively, these data demonstrate that IDH1^{WT} and IDH1^{mut} tumours are defined by unique, co-occurring genomic and transcriptomic profiles that exist in varying

proportions among glioma subtypes and highlight the utility of SCRAM for defining transcribed mutations and integrated cellular states in human glioma.

Previous observations have indicated that spatially-distinct regions within individual tumours possess unique transcriptomic and genomic signatures[16]; therefore, we sought to spatially resolve the co-occurring cell types identified in our glioma dataset by comparing tumor cells surgically resected from the leading edge with those of the tumor core. Analysis of each Seurat-generated cluster revealed that clusters were diverse and frequently featured both tumour and non-tumour cells with similar transcriptional expression patterns (e.g., astrocytes and astrocyte-like tumour cells). The largest tumour cell cluster in our human dataset (Cluster 1) contained cells that were uniformly annotated as astrocytes and featured various co-occurring chromosome 5p, 5q, 7p, 7q, and 17q amplifications and chromosome 10p, 10q, and 22q losses (**Figs. 3A–D**). Visualization of co-occurring CNVs by patient showed that IDH1^{WT} tumour cells in the leading edge featured fewer variations of co-occurring chromosomal rearrangements than tumour cells in the core (**Fig. 3E**). This finding suggests that clonal tumour cells in the leading edge emerge from specific glioma cell subclones residing in the tumour core and is further supported by lineage-tracing studies showing that leading edge cells emanate from more primitive cell types in the tumour core (**Figs. 3F–H**). Using RNA velocity pseudotime analysis[17], we found that these astrocytic tumour cells emanate from stem cell–like tumour cells in Cluster 23 and transition through an intermediate cell type found primarily in Cluster 3 **(Figs. S6A–D**). These intermediate cell types possess neurodevelopmentally restricted transcriptional profiles resembling those of embryonic astrocytes or radial glia while retaining the frequently co-occurring CNV annotations observed in Cluster 1. By contrast, the progenitor– and stem cell–like cells found in Cluster 23 feature only a single CNV occurrence and are characterized by the addition of primitive, co-occurring cell identities, including neural stem cell (NSC) and glioma stem cell (GSC), as well as oligodendrocyte annotation (**Figs. 3I–L**). These observations

suggest that astrocyte-like tumour cells with widespread chromosomal anomalies derive from a chromosomally intact stem cell–like cell population featuring transcriptional profiles resembling those of oligodendrocytes. These cells transition through an intermediate cell state in which stem cell signatures are lost and pervasive co-occurring CNVs are gained (**Fig. 3M**). Synchronously, SCRAM identified analogous populations of glioma cells in our scRNA-seq dataset from our piggyBac transposase–based *in utero* electroporation (pB-IUE) glioma model, which yields green fluorescent protein (GFP)-labelled *de novo* tumours in immunocompetent mice (**Figs. S6E–H**). These combined analyses identified a compendium of individual cellular states identified by SCRAM that parallel neurodevelopmental trajectories and defined co-occurring spatiotemporal hierarchies.

SCRAM reveals APC-like tumour cells in astrocytoma

Our prior analyses identified co-occurring neurodevelopmental cellular states within glioma cell transcriptomes, leading us to investigate whether these tumours also contain cellular signatures derived from non-neural lineages. We found 229 cells in Cluster 19 characterized by both tumour cell and APC annotations, which we termed APC-like tumour cells (ALTs). ALTs are rare (<1%) and unique to astrocytoma tumours in both $IDH1^{WT}$ and $IDH1^{mut}$ patients and frequently feature CNVs, cycling progenitor cell annotation, and high expression of the activated APC marker *CD83*[18] and major histocompatibility complex (MHC) I and II genes[19] (**Figs. 4A–D; Fig. S7A**). Many immune cell subtypes actively surveil the tumour microenvironment, where they engulf and display tumour antigens through processes of antigen presentation[20]. To confirm that ALTs were not artefacts representing immune cells phagocytosing tumour cells, we examined expression of the immune cell lineage marker *PTPRC* (CD45, **Fig. S7B**) and found no *PTPRC* expression in 69% of ALTs. SCRAM also identified an analogous population of *Ptprc*-negative ALTs in mouse glioma, which featured high *GFP* and *Cd83* expression (**Figs. S7C–E**). These

data suggest the existence of a rare CNV-altered tumour cell population in high-grade astrocytoma, characterized by APC transcriptional signatures, and confirm the existence of a parallel cell population in our pB-IUE model.

ALTs promote activation of CD8+ T cells

The former observations uncovered a rare population of ALTs in human glioma that was similarly detected in our pB-IUE model of murine glioma. Because pB-IUE tumors arise *de novo* in an immunocompetent setting, we exploited GFP-labelling of glioma cells and used multispectral imaging flow cytometry to experimentally discern if ALTs can be confirmed *in vivo*. Using this imaging platform, we identified two populations of $CD83^{+}GFP^{+}$ cells of interest. The first population featured dendrite-like projections and punctate GFP expression (**Fig. S8A**), which was located both intracellularly and adjacent to CD83 on the cell surface. Past studies employing this imaging modality to examine phagocytosis in live cells[21] describe this expression pattern as indicative of $CD83^{+}$ immune cells actively phagocytosing or displaying GFP^{+} tumour antigen on their surface. A second population of $CD83^{+}GFP^{+}$ cells was characterized by high, diffuse, intracellular GFP expression, a hallmark of targeted cells in the pB-IUE model[22], and therefore represented SCRAM-identified ALTs (**Fig. 4E; S8B–D**). Subsequent analysis also revealed a rare number of events wherein $CD83^{-}GFP^{-}$ cells were bound to GFP^{+} tumour cells at a $CD83^{+}$ interface (**Fig. S8E**), further implicating CD83 as a mediator of tumour–host cell interactions in glioma. These imaging studies confirmed the existence of an endogenous $CD83^{+}GFP^{+}$ ALT cell population in the pB-IUE glioma model, similar to the population identified by SCRAM in humans and mice.

Because CD83 is required for antigen presentation in non-tumour immune cells, we examined how changes to tumor cell CD83 expression affect *in vivo* tumour progression. We used CRISPR/Cas9 technology to generate CD83 loss-of-function ($CD83^{KO}$) pB-IUE tumours and separately used murine *Cd83* overexpression to generate CD83 gain-of-function ($CD83^{OE}$) pB-

IUE tumours **(Figs. S8F,G)**. Kaplan–Meier survival analysis revealed that CD83^{KO} tumours were associated with reduced survival times, whereas CD83^{OE} tumours were associated with extended survival compared with control tumours (**Fig. 4F**). Age-matched CD83^{OE} tumours were smaller than control tumours, whereas CD83^{KO} tumours appeared significantly larger (**Figs. 4G,H**). Cell proliferation assays using Ki67 showed that CD83^{OE} tumours were less proliferative than age-matched CD83^{KO} and control tumours; however, no difference in proliferation was observed between control and CD83^{KO} tumours (**Figs. S8H,I**). Considering the worse survival outcomes associated with CD83^{KO} tumours, we analysed the number of nuclei per tumour field of view and found that CD83^{KO} tumours contained nearly 50% more cells than control tumours (**Fig. S8J**), raising the possibility that impaired immune clearance of tumour cells may account for CD83^{KO} phenotypes. These collective observations demonstrate that intra-tumoural CD83 expression modulates disease progression in mouse glioma and suggest that tumour extrinsic mechanisms may contribute to poor survival outcomes when CD83 expression is lost.

CD83 directs T cell responses by enhancing MHC gene expression and enabling antigen presentation by APCs[23]; therefore, we characterized how changes in CD83 expression levels in tumour cells affect T cell responses in glioma. We derived glioma cell lines from pB-IUE tumours and performed co-culture experiments with naïve CD8^{+} T cells (**Fig. 4I**). Following 1 week of co-culture, T cells were harvested for imaging flow cytometry, which revealed that CD83^{OE} co-cultures had the largest CD3^{+}CD8^{+} population (**Fig. 4J**). Closer examination uncovered a subset of CD3^{-}CD8^{+} cells in CD83^{KO} co-cultures, greater than 90% of which expressed the naïve T cell marker C–C chemokine receptor type 7 (CCR7) and greater than 76% of which co-expressed the activated marker CD25 (**Fig. 4K**). Prior studies show that CD3 loss reduces T cell expansion[24,25], and CCR7 loss is required for the acquisition of cytotoxic functions in CD8^{+} effector memory T cells[26,27]. Additionally, a subset of CD8^{+}CCR7^{+}CD25^{+} T cells has been implicated as potent immunosuppressive mediators[28], suggesting that

$CD3^{-}CD8^{+}CCR7^{+}$ T cells may contribute to subpar T cell responses in $CD83^{KO}$ tumours. Consistent with these data, enzyme-linked immunosorbent assay (ELISA) analyses of co-culture media revealed that both $CD83^{OE}$ and $CD83^{KO}$ co-cultures showed increased production of the T cell–activating cytokines interferon-gamma (IFNγ) and tumour necrosis factor-alpha (TNFα)[29,30], but only $CD83^{OE}$ co-cultures showed increased interleukin (IL)-2, which is required for memory and effector T cell subsets[31] (**Figs. 4L,M**). Our scRNA-seq analyses of CD83-altered tumours confirmed that $CD83^{OE}$ tumours are enriched for T cell–activating cytokines (**Fig. 4N**) and that T cells from $CD83^{KO}$ tumours displayed increased expression of anergic and regulatory T cell markers. In contrast, T cells from $CD83^{OE}$ tumours showed high expression of *CD44*, a prominent memory and effector T cell activation marker[32] (**Fig. 4O**). Notably, *in vitro* 5-ethynyl-2′-deoxyuridine (EdU) assays revealed that $CD83^{OE}$ tumour cells were intrinsically more proliferative than control tumour cells and had similar proliferation rates to $CD83^{KO}$ tumour cells (**Figs. 4P,Q**). We confirmed this result through scRNA-seq cell cycle scoring of CD83-altered tumours, which showed increased expression of proliferation markers in $CD83^{OE}$ and $CD83^{KO}$ tumour cells compared with control tumour cells (**Figs. S8K–M**). Combined with our *in vivo* proliferation and survival study results, these findings suggest that T cell–CD83 interactions in $CD83^{OE}$ tumours promote tumour cell clearance and counteract glioma cell proliferation, thus ameliorating poor survival outcomes (**Fig. 4R**). These results demonstrate that modulation of CD83 expression in tumours can direct glioma progression through both cell autonomous proliferation effects and cell non-autonomous responses mediated by T cell–dependent changes to the cytokine milieu. Moreover, these studies emphasize the ability of SCRAM to identify rare, co-occurring tumour cell populations that may contribute to tumour biology.

Functional neuronal-like tumour cells are unique to *IDH1* mutant glioma

Parallel analyses using SCRAM revealed that most tumour cells from $IDH1^{mut}$ samples mapped to Cluster 4, which displayed a high density of *IDH1* mutations and featured chromosome 1p19q

co-deletions in oligodendroglioma patients (**Figs. 5A–C**). We found that 40% of cells (4324 out of 10739 cells) with CNV or GSC annotation had co-occurring cell type annotations of mature neurons, GABAergic neurons and/or synaptic neurons, as well as oligodendrocytes and OPCs (**Fig. 5D**); in contrast, only 18 of 349 tumour cells had co-occurring neuronal signatures in IDH1^{WT} samples. SCRAM identified a similar population of neuronal-like tumour cells (NLTs) in our mouse glioma dataset (**Figs. S9A,B**), which prompted us to further investigate these cell types.

To validate the existence of NLTs, we performed whole-cell patch clamp recordings, followed by scRNA-seq (Patch-seq), on brain slices resected from the tumour cores of two IDH1^{mut} glioma specimens (**Fig. 5E**). We recorded from 53 total cells; 31 were used to recover high-quality RNA for scRNA-seq, and 20 were preserved with biocytin for morphological analysis (**Figs. 5F–H; Figs. S10A–H**). Of these cells, 27 displayed electrophysiological and morphological properties consistent with either glia or neurons in the non-tumour brain[33,34], whereas 26 cells displayed select neuronal electrophysiological properties but were morphologically consistent with glia, and therefore were presumed to be NLTs. These presumptive NLTs had higher input resistances than either typical neurons or glia (**Fig. 6A**) and had the capacity to fire single, small action potentials (APs; **Figs. 6B,C**), signifying that the acquired transcriptional signatures of these cells correlated with neuronal functional characteristics. Prior work describes similar electrophysiological properties for early-stage, post-mitotic, newborn neurons, implicating hyperexcitability, high input resistance, and the firing of single APs as defining features of this developmental stage[35]. Newborn neurons also feature high GABA receptor levels[36,37], which are also expressed in NLTs, and SCRAM identified several cells with annotations for both GABAergic neurons and IDH1^{mut} tumour cells. Our Patch-seq results revealed the presence of the canonical *IDH1R132H* mutation in five of 15 NLTs, confirming that these cells were tumour (**Fig. 6D; Figs. S11A**). Subsequent cell type enrichment analysis of Patch-seq data using the

EnrichR tool[6,38] demonstrated that NLTs are transcriptionally similar to glia, showing enrichment for embryonic, astrocytic, and OPC gene sets (**Figs. 6E,F**). Using the SCRAM *de novo* marker tool, we identified *SOX11* as an NLT marker in both Patch-seq and scRNA-seq datasets (**Figs. S11B,C**). When we attempted to record from an IDH1^{WT} glioblastoma core sample, very few cells were patchable due to gliosis and necrosis; however, all three cells recorded were electrophysiologically consistent with glia (**Fig. S10H**). Using *in vivo* modelling, whole-cell recordings were obtained for GFP^{+} tumour cells from control pB-IUE model mice, revealing an analogous population of NLTs (**Figs. S11D,E**). Taken together, these human and mouse studies confirm the existence of NLTs featuring transcriptional and electrophysiological properties similar to but distinct from neurons as a defining feature of human IDH1^{mut} glioma.

We mapped the 31 Patch-seq cells to our human glioma scRNA-seq dataset and found that all 15 NLTs examined by Patch-seq mapped to GABAergic neurons with co-occurring GSC, OPC, or oligodendrocyte annotations (**Figs. 6F,G**). Although only five Patch-seq NLTs presented with the canonical *IDH1R132H* mutation, 12 NLTs presented with *SUZ12, KIF27, GTF2I*, *PMS2,* or non-canonical *IDH1* mutations (**Figs. S11F,G**), all of which were previously identified in both IDH1^{WT} and IDH1^{mut} patients in our scRNA-seq dataset (**Fig. S3H**). Using Patch-seq mapping, together with principal component analysis (PCA) and SNV analysis, we divided the 31 Patch-seq cells into subclasses based on electrophysiology profiles, PCA clustering, mapping to our SCRAM-annotated scRNA-seq dataset, SNV incidence, and cell type marker expression (**Figs. 6E–J; Fig. S12**). Employing this strategy, we uncovered 10 cells with electrophysiological properties similar to either pyramidal cells or interneurons that mapped strongly to NLT-annotated cells, five of which featured similar mutational profiles to NLTs. Unlike early-stage newborn NLTs, which are electrophysiologically distinct from differentiated interneurons and pyramidal cells, these mutation-bearing pyramidal cell– and interneuron-like cells, which we refer to as differentiated NLTs, were not electrophysiologically distinct from non-tumour neurons; however, they trended towards input resistances and AP amplitudes between those of

non-tumour neurons and newborn NLTs, and had high maximal AP firing rates (**Figs. S13A–C**). In addition, differentiated NLTs were morphologically similar to non-tumour neurons but mapped to both non-tumour neuronal cell types and NLTs in our scRNA-seq dataset, whereas newborn NLTs did not show strong neuronal transcriptional profiles. Examination of Patch-seq transcriptional profiles revealed proliferation markers were only expressed by newborn and differentiated NLTs, suggesting that NLTs represent the major proliferative constituents in these tumours (**Fig. 6J**). We found that embryonic astrocytic genes were enriched in differentiated NLTs, which also feature high expression of RNA polymerase III, the overexpression of which has been linked to DNA damage and cancer[39,40] (**Fig. 6J; Figs. S13D,E**). These observations suggest that more than one NLT cell type exists and that these NLT cell types collectively form a neurodevelopmental spectrum paralleling the processes of neuronal differentiation. Whether differentiated NLTs represent astrocyte-derived tumour cells that have acquired the transcriptional and electrophysiological properties of differentiated neuronal subtypes or are indicative of non-tumour neurons undergoing transcriptomic remodelling and transformation remains an important question, the answer to which could shed light on the origins of glioma cells and should be further explored in future studies.

Discussion

A computational framework for defining genomic and transcriptional states

By 2040 the number of new cancer cases per year will be 29.5 million worldwide, more than half of which will end in cancer-related deaths[41]. While advances in single-cell sequencing technologies have given scientists the opportunity to examine individual cells in unprecedented detail, the power of these data has yet to be harnessed by computational platforms capable of resolving these profiles on a cell-by-cell basis. To address this unmet need, we developed SCRAM, which we report here as the first computational algorithm of its kind capable of defining

integrated co-occurring, genomic and transcriptomic features from single cell datasets. In this report, we employed SCRAM using a curated brain tumour-specific cell type marker list to elucidate two previously unreported glioma cell types; however, our pipeline can be easily expanded for use in any cancer, non-oncologic, or developmental context and thus represents a new computational platform that can be used to study human and mouse biology.

ALTs enable antitumor T cell responses

Owing in part to the existence of a highly immunosuppressive tumour microenvironment, immunotherapy trials for glioma have been largely unsuccessful, with little to no overall survival benefits[42,43]. Prior tumour immunology research has characterized the molecular mechanisms mediating this immunosuppressive environment in glioma, implicating anergic and regulatory T cells as important mediators[44,45]. Researchers have shown that tumour cells present endogenous antigens via MHC, and speculated that MHC loss in cancer impairs naïve T cell priming and subsequent antitumour cytotoxic T cell responses[46–50]. Considered alongside prior work confirming CD83 as a regulator of MHC expression[51,52], our data implicate CD83 as a mediator of antigen presentation by glioma cells and suggest that CD83 loss promotes immunosuppressive T cell responses by impairing glioma cell antigen presentation. Our imaging flow cytometry experiments confirmed that GFP^+ tumour cells are actively surveilled by the surrounding immune environment, implicating downstream immunosuppressive responses as likely culprits for poor survival outcomes. Whether changes to the proportions of activated $CD8^+$ T cells in CD83-altered tumours correlate with their abilities to recognize and destroy glioma cells remains unanswered and should be the focus of future inquiries.

NLTs are a hallmark of $IDH1^{mut}$ glioma

Over the past decade, the emerging field of cancer neuroscience has elucidated how glioma cells interact with surrounding neural networks to direct disease progression[53,54]. Prior studies

have reported that human glioma cells receive synaptic inputs from the surrounding neuronal circuitry[55–57]. Our studies build upon past reports by suggesting that SCRAM-identified NLTs may communicate with peri-tumoural neurons by directing outgoing electrochemical information in the form of APs. These data suggest that dysregulated electrophysiological activity in the glioma-bearing brain may originate from tumour cells able to initiate and propagate outgoing neurochemical signals. Importantly, NLTs were the only cells expressing proliferation markers in our Patch-seq dataset, suggesting that NLTs are important contributors to both the neurophysiological and proliferative characteristics of glioma. Clinically, IDH1^{mut} glioma frequently presents with seizures[58], raising the possibility that NLTs may contribute to both hyperexcitable and proliferative phenotypes in these tumors.

Our studies also uncovered a SNV-bearing population of neurons featuring transcriptomic profiles consistent with both non-tumour neurons and tumour cells, which we termed differentiated NLTs. The existence of these cells brings into focus the longstanding and controversial topic of tumour cell origins. Prior work has theorized that GSCs arise from OPCs[59–61], which is supported by our observations that newborn NLTs are enriched for OPC and GSC signatures. However, by layering our SNV analysis onto both transcriptional and electrophysiological profiling, we found that differentiated NLTs have a lower mutational burden than other tumour cells. These data imply that differentiated NLTs may not derive from the tumour but may instead represent a population of peri-tumoural neurons undergoing malignant transformation. Future investigations remain necessary to confirm the origins of differentiated NLTs, which will improve the current understanding of how tumor cells arise in malignant glioma.

Acknowledgements

This work was supported by grants from the NIH (R01NS071153 to B.D., R01NS124093 to B.D. and G.R., R01CA223388 to B.D, R01NS094615 to G.R.). R.N.C. is supported by grants from the NIH (5T32HL92332-15, F31CA265156, and F99CA274700). The Baylor College of Medicine Single Cell Genomics Core is supported by NIH Shared Instrument Grants (S10OD023469, S10OD025240), P30EY002520, and CPRIT grant RP200504. Schematics were created using Biorender.com. The Cytometry and Cell Sorting Core at Baylor College of Medicine is supported by funding from the CPRIT Core Facility Support Award (CPRIT-RP180672), the NIH (CA125123 and RR024574), and the assistance of Joel M. Sederstrom. BioSorter is supported by NIH grant S10 OD025251.

Data availability

The Patch-seq and scRNA-seq datasets generated during this study will be made available through the NCBI Gene Expression Omnibus (GEO) website. All other study data are included in the article and/or supporting information.

Code availability

The source code of SCRAM will be available upon publication.

Author contributions

R.N.C. and A.S.H. are responsible for conception of this project, the study and pipeline design, and interpretation of the results. R.N.C. performed all pB-IUE surgeries, *in vitro* and FACS experiments, immunostaining, and statistical analyses and prepared all scRNA-seq samples from humans and mice with assistance from M.F.M., and A.S.H. wrote the code for the SCRAM pipeline. Q.M. and J.J. performed all human electrophysiology and Patch-seq experiments. J.M. performed the two-photon and widefield imaging studies in mice and subsequent analyses. I.A. performed all mouse electrophysiology and respective analyses. R.N.C., A.O.H., and A.S.H. performed bioinformatics analyses on human and mouse scRNA-seq datasets. A.C. maintained

all mouse colonies and assisted with tissue harvesting and fixation. B.L., Z.L., D.C, E.L.F., Y.K., P.H., and A.R. provided experimental support for *in vitro* cell culture, immunohistochemistry, immunofluorescence, immunocytochemistry, and surveyor experiments. C.M. performed histopathological diagnoses of mouse tumours. A.J. and G.R. identified and obtained consent from patients for the study. R.N.C. and A.S.H prepared the manuscript. J.N., X.J., B.D., and G.R. contributed to the manuscript with feedback from all authors.

Declaration of Interests

The authors declare no competing interests.

Contact for reagent and resource sharing

Dr. Akdes Serin Harmanci (akdes.serinharmanci@bcm.edu) is the lead contact for reagent and resource sharing. All published reagents will be shared on an unrestricted basis; reagent requests should be directed to the corresponding author.

Figures & Figure Legends

Figure 1

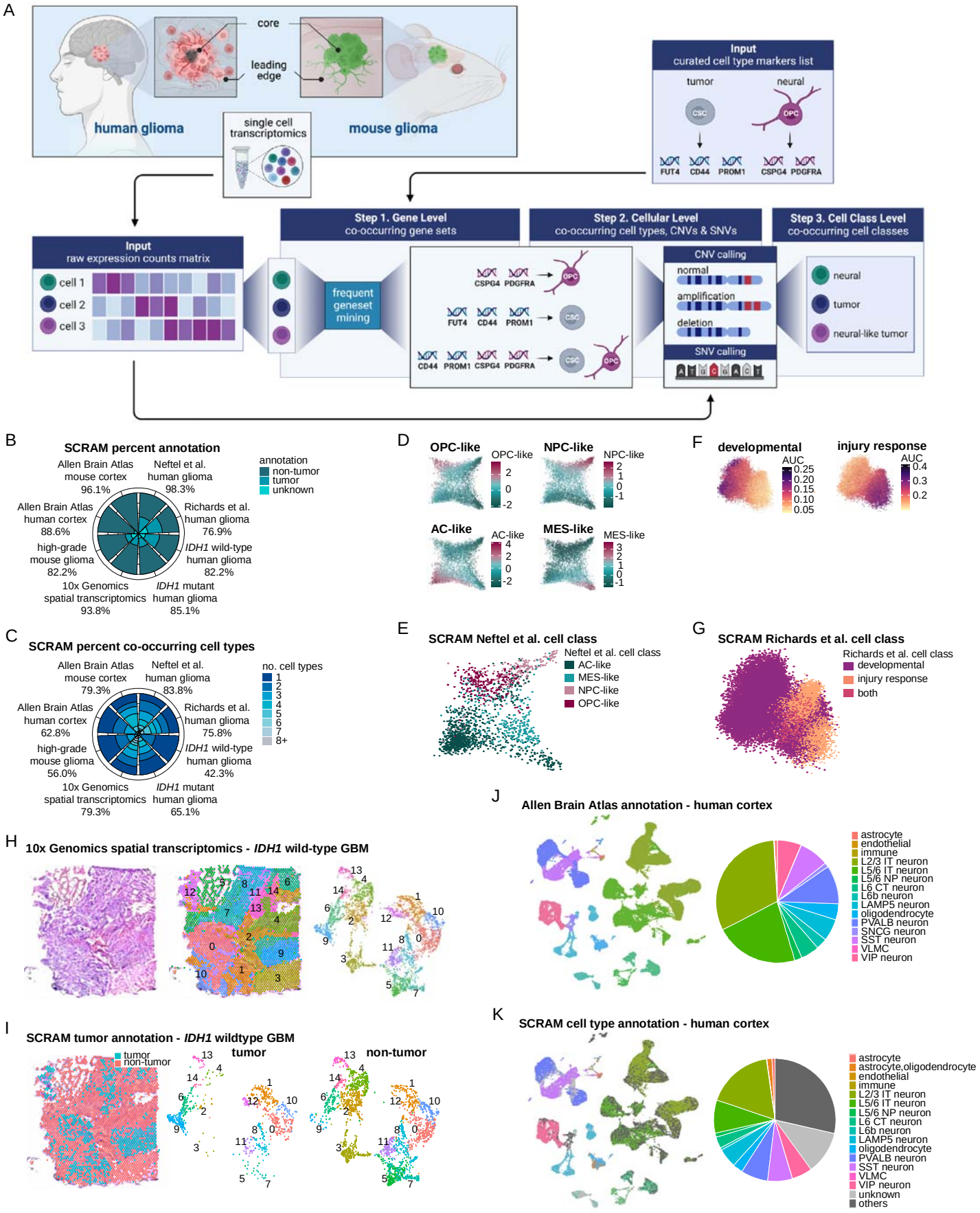
A
core
leading edge
human glioma
single cell transcriptomics
mouse glioma
Input
curated cell type markers list
tumor
neural
CSC
OPC
FUT4 CD44 PROM1
CSPG4 PDGFRA
Input
raw expression counts matrix
cell 1
cell 2
cell 3
Step 1. Gene Level
co-occurring gene sets
frequent geneset mining
Step 2. Cellular Level
co-occurring cell types, CNVs & SNVs
CNV calling
normal
amplification
deletion
SNV calling
Step 3. Cell Class Level
co-occurring cell classes
neural
tumor
neural-like tumor
B
SCRAM percent annotation
annotation
non-tumor
tumor
unknown
Allen Brain Atlas mouse cortex 96.1%
Neftel et al. human glioma 98.3%
Richards et al. human glioma 76.9%
IDH1 wild-type human glioma 82.2%
IDH1 mutant human glioma 85.1%
10x Genomics spatial transcriptomics 93.8%
high-grade mouse glioma 82.2%
Allen Brain Atlas human cortex 88.6%
C
SCRAM percent co-occurring cell types
no. cell types
1
2
3
4
5
6
7
8+
Allen Brain Atlas mouse cortex 79.3%
Neftel et al. human glioma 83.8%
Richards et al. human glioma 75.8%
IDH1 wild-type human glioma 42.3%
IDH1 mutant human glioma 65.1%
10x Genomics spatial transcriptomics 79.3%
high-grade mouse glioma 56.0%
Allen Brain Atlas human cortex 62.8%
D
OPC-like
NPC-like
AC-like
MES-like
E
SCRAM Neftel et al. cell class
Neftel et al. cell class
AC-like
MES-like
NPC-like
OPC-like
F
developmental
injury response
AUC
G
SCRAM Richards et al. cell class
Richards et al. cell class
developmental
injury response
both
H
10x Genomics spatial transcriptomics - IDH1 wild-type GBM
I
SCRAM tumor annotation - IDH1 wildtype GBM
tumor
non-tumor
J
Allen Brain Atlas annotation - human cortex
astrocyte
endothelial
immune
L2/3 IT neuron
L5/6 IT neuron
L5/6 NP neuron
L6 CT neuron
L6b neuron
LAMP5 neuron
oligodendrocyte
PVALB neuron
SNCG neuron
SST neuron
VLMC
VIP neuron
K
SCRAM cell type annotation - human cortex
astrocyte
astrocyte,oligodendrocyte
endothelial
immune
L2/3 IT neuron
L5/6 IT neuron
L5/6 NP neuron
L6 CT neuron
L6b neuron
LAMP5 neuron
oligodendrocyte
PVALB neuron
SST neuron
VLMC
VIP neuron
unknown
others

Figure 1. SCRAM reliably assigns cell type annotations to single-cell RNA-sequencing datasets on a cell-by-cell basis. (A) Schematic representation of the Single-Cell Rule Association Mining (SCRAM) pipeline. (B) Percentages of SCRAM-annotated cells assigned to non-tumour, tumour, or unknown cell types across eight datasets. Percentages shown below dataset names indicate the total cell percentages assigned to each cell type annotation using SCRAM. (C) Percentages of SCRAM-annotated cells by the number of co-occurring cell types. Percentages shown below dataset names indicate cells with more than one cell type annotation. (D) Reproduction of meta-modules from Neftel et al.[5], showing astrocyte-like (AC-like), oligodendrocyte precursor cell–like (OPC-like), mesenchymal-like (MES-like), or neural precursor cell–like (NPC-like) cellular states. (E) Meta-module of SCRAM-identified tumour cells from Neftel et al. dataset. (F) Reproduction of cell state modules from Richards et al.[9], showing developmental and injury response programmes. (G) SCRAM-assigned developmental and injury response cell classes for the Richards et al. dataset. (H) Haematoxylin and eosin staining and corresponding Seurat clusters are shown for the 10X Genomics spatial transcriptomics *IDH1*–wild-type ($IDH1^{WT}$) glioblastoma (GBM) dataset. (I) SCRAM-assigned tumour and non-tumour annotations for the 10X Genomics spatial transcriptomics $IDH1^{WT}$ GBM dataset show tumour cells are embedded throughout non-tumour tissue. Seurat clusters separated by tumour and non-tumour annotations show clusters comprised of tumour and non-tumour cells. (J) Cell type annotation for human cortex dataset provided by Allen Brain Atlas. (K) SCRAM-assigned cell type annotation for the Allen Brain Atlas human cortex dataset reveals co-occurring cell identities (dark grey) and unknown transcriptional cell states (light grey).

446 **Figure 2**

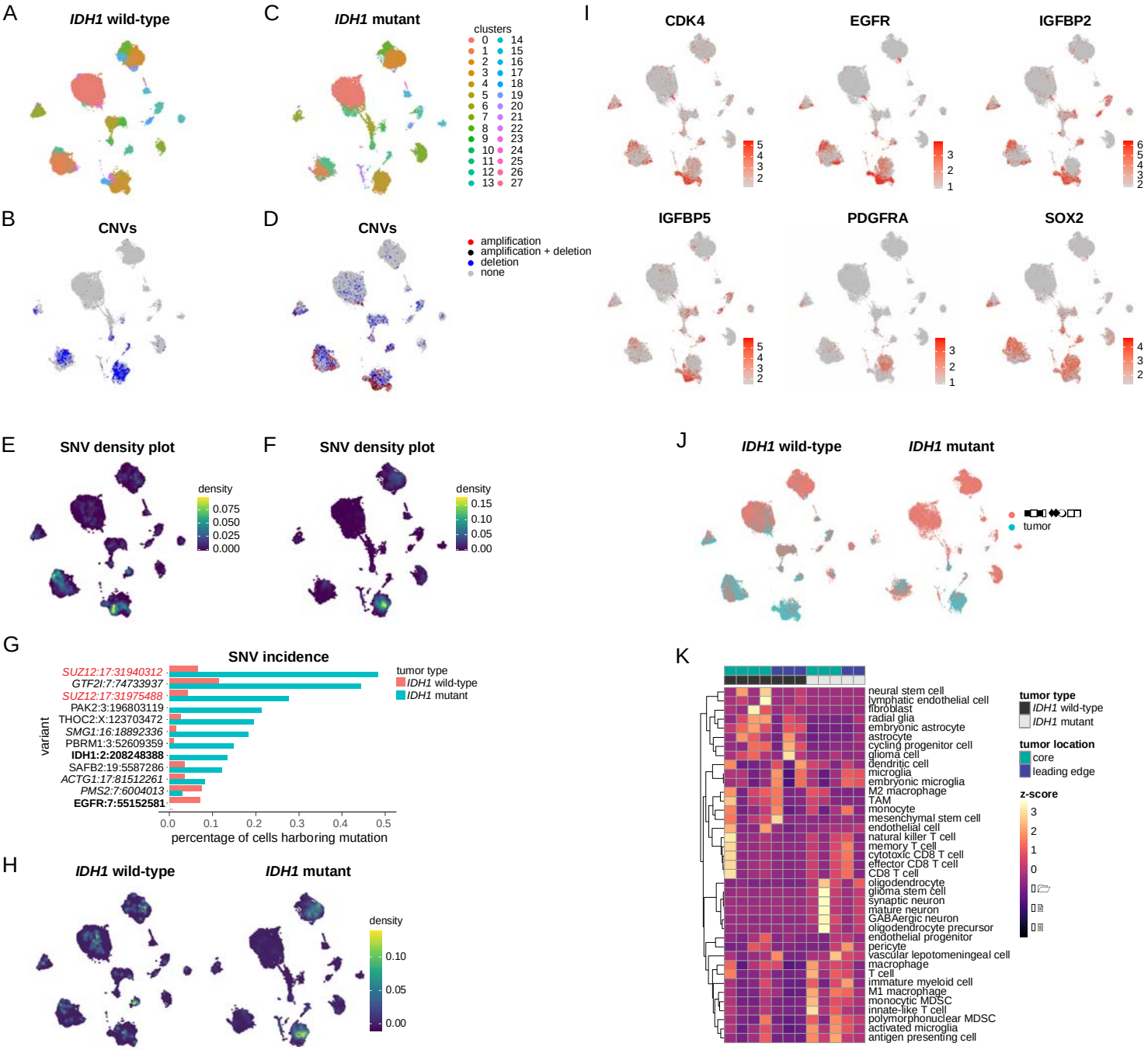
A
IDH1 wild-type
C
IDH1 mutant
clusters
0 1 2 3 4 5 6 7 8 9 10 11 12 13 14 15 16 17 18 19 20 21 22 23 24 25 26 27
I
CDK4
EGFR
IGFBP2
IGFBP5
PDGFRA
SOX2
B
CNVs
D
CNVs
amplification
amplification + deletion
deletion
none
E
SNV density plot
density
0.075
0.050
0.025
0.000
F
SNV density plot
density
0.15
0.10
0.05
0.00
J
IDH1 wild-type
IDH1 mutant
tumor
G
SNV incidence
SUZ12:17:31940312
GTF2I:7:74733937
SUZ12:17:31975488
PAK2:3:196803119
THOC2:X:123703472
SMG1:16:18892336
PBRM1:3:52609359
IDH1:2:208248388
SAFB2:19:5587286
ACTG1:17:81512261
PMS2:7:6004013
EGFR:7:55152581
variant
tumor type
IDH1 wild-type
IDH1 mutant
0.0 0.1 0.2 0.3 0.4 0.5
percentage of cells harboring mutation
H
IDH1 wild-type
IDH1 mutant
density
0.10
0.05
0.00
K
neural stem cell
lymphatic endothelial cell
fibroblast
radial glia
embryonic astrocyte
astrocyte
cycling progenitor cell
glioma cell
dendritic cell
microglia
embryonic microglia
M2 macrophage
TAM
monocyte
mesenchymal stem cell
endothelial cell
natural killer T cell
memory T cell
cytotoxic CD8 T cell
effector CD8 T cell
CD8 T cell
oligodendrocyte
glioma stem cell
synaptic neuron
mature neuron
GABAergic neuron
oligodendrocyte precursor
endothelial progenitor
pericyte
vascular lepotomeningeal cell
macrophage
T cell
immature myeloid cell
M1 macrophage
monocytic MDSC
innate-like T cell
polymorphonuclear MDSC
activated microglia
antigen presenting cell
tumor type
IDH1 wild-type
IDH1 mutant
tumor location
core
leading edge
z-score
3
2
1
0

Figure 2. Integrated RNA-inferred genomic and transcriptomic cellular states reveal unique molecular signatures in *IDH1*–wild-type and *IDH1*-mutant glioma. (A) Seurat clusters are shown for 157,316 cells from *IDH1* wild-type ($IDH1^{WT}$) glioma patients (n=4). (B) Feature plot showing total copy-number variant (CNV) calls by Single-Cell Rule Association Mining (SCRAM) for $IDH1^{WT}$ tumours. (C) Seurat clusters are shown for 37,747 cells from *IDH1*-mutant (*IDH1*^{mut}) glioma patients (n=3). (D) Feature plot showing total CNV calls by SCRAM for $IDH1^{mut}$ tumours. (E) Density plot showing single-nucleotide variant (SNV) density for rare and COSMIC variants in $IDH1^{WT}$ glioma. (F) Density plot showing SNV density for rare and COSMIC variants in $IDH1^{mut}$ glioma. (G) Bar plot of the top 12 most frequent SNVs. Plot shows the percentage of cells harbouring rare and COSMIC SNVs in $IDH1^{WT}$ and $IDH1^{mut}$ glioma; italics denote genes with known pseudogenes; bold denotes known driver genes in glioma. (H) Density plot showing either *SUZ12* mutations or the *SUZ12P1* pseudogene detected in $IDH1^{WT}$ and $IDH1^{mut}$ samples. (I) Feature plots for tumour cell markers used to assign tumour annotation. (J) SCRAM-assigned tumour annotations are shown for $IDH1^{WT}$ and $IDH1^{mut}$ glioma. (K) Heatmap showing enrichment for SCRAM-assigned cell types by tumour type and sample location; z-score for expression of cell types is shown.

463 **Figure 3**

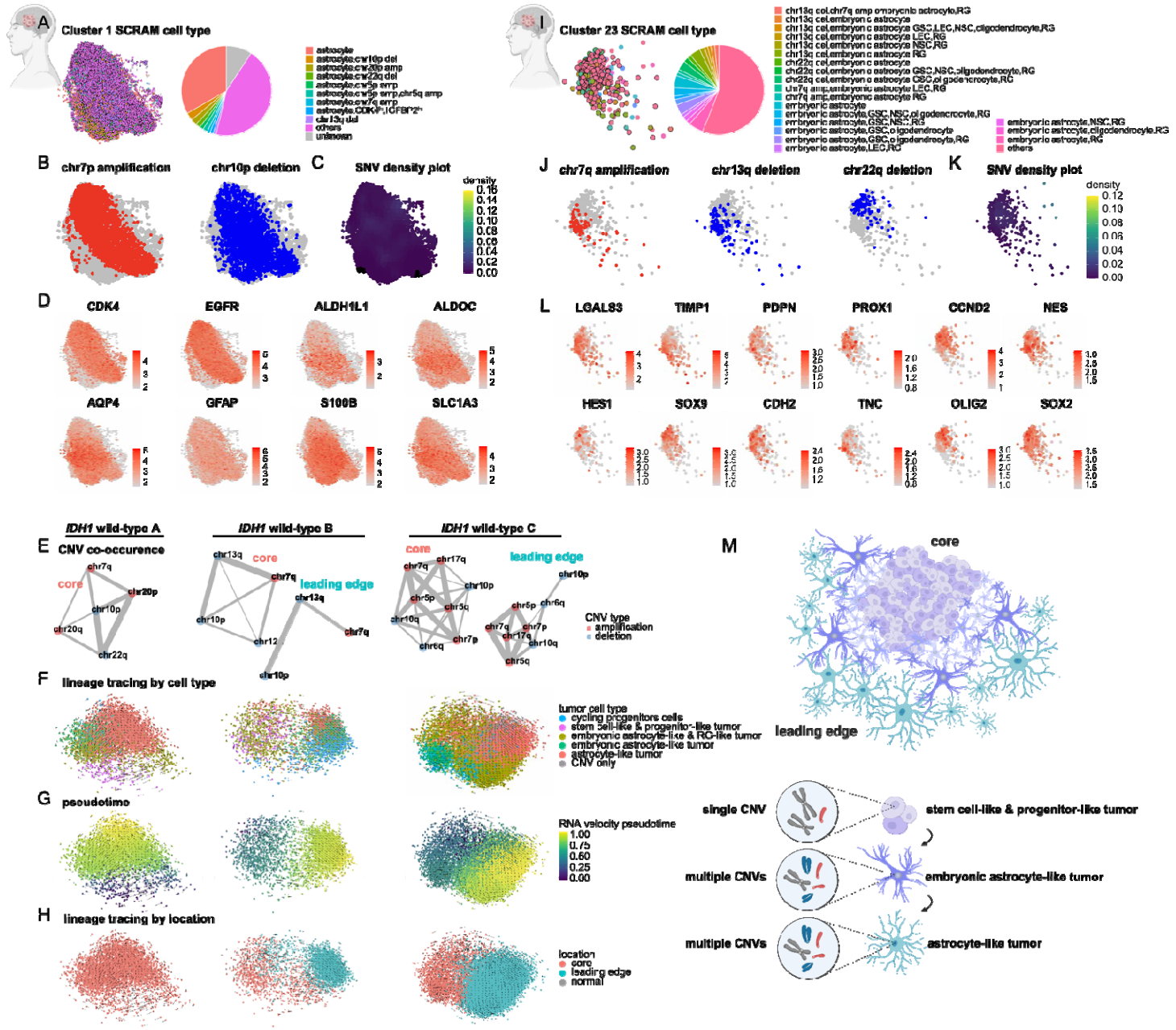
A
Cluster 1 SCRAM cell type
astrocyte
astrocyte,chr10p del
astrocyte,chr20p amp
astrocyte,chr22q del
astrocyte,chr5p amp
astrocyte,chr5p amp,chr5q amp
astrocyte,chr7q amp
astrocyte,CDK4+,FGFR2+
chr13q del
others
unknown
I
Cluster 23 SCRAM cell type
chr13q cel,chr7q amp embryonic astrocyte,RG
chr13q cel,embryonic astrocyte
chr13q cel,embryonic astrocyte GSC,LEC,NSC,oligodendrocyte,RG
chr13q cel,embryonic astrocyte LEC,RG
chr13q cel,embryonic astrocyte NSC,RG
chr13q cel,embryonic astrocyte RG
chr22q cel,embryonic astrocyte
chr22q cel,embryonic astrocyte GSC,NSC,oligodendrocyte,RG
chr22q cel,embryonic astrocyte GSC,oligodendrocyte,RG
chr7q amp,embryonic astrocyte LEC,RG
chr7q amp,embryonic astrocyte RG
embryonic astrocyte
embryonic astrocyte,GSC,NSC,oligodendrocyte,RG
embryonic astrocyte,GSC,NSC,RG
embryonic astrocyte,GSC,oligodendrocyte
embryonic astrocyte,GSC,oligodendrocyte,RG
embryonic astrocyte,LEC,RG
embryonic astrocyte,NSC,RG
embryonic astrocyte,oligodendrocyte,RG
embryonic astrocyte,RG
others
B
chr7p amplification
chr10p deletion
C
SNV density plot
density
0.16
0.14
0.12
0.10
0.08
0.06
0.04
0.02
0.00
J
chr7q amplification
chr13q deletion
chr22q deletion
K
SNV density plot
density
0.12
0.10
0.08
0.06
0.04
0.02
0.00
D
CDK4
EGFR
ALDH1L1
ALDOC
AQP4
GFAP
S100B
SLC1A3
L
LGALS3
TIMP1
PDPN
PROX1
CCND2
NES
HES1
SOX9
CDH2
TNC
OLIG2
SOX2
E
IDH1 wild-type A
CNV co-occurence
core
chr7q
chr20p
chr10p
chr20q
chr22q
IDH1 wild-type B
chr13q
core
chr7q
leading edge
chr13q
chr10p
chr12
chr7q
chr10p
IDH1 wild-type C
core
chr7q
chr17q
chr10p
chr5p
chr3q
chr10q
chr6q
chr7p
leading edge
chr10p
chr5p
chr6q
chr7q
chr7p
chr17q
chr10q
chr5q
CNV type
amplification
deletion
M
core
leading edge
F
lineage tracing by cell type
tumor cell type
cycling progenitors cells
stem cell-like & progenitor-like tumor
embryonic astrocyte-like & RC-like tumor
embryonic astrocyte-like tumor
astrocyte-like tumor
CNV only
G
pseudotime
RNA velocity pseudotime
1.00
0.75
0.50
0.25
0.00
H
lineage tracing by location
location
core
leading edge
normal
single CNV
stem cell-like & progenitor-like tumor
multiple CNVs
embryonic astrocyte-like tumor
multiple CNVs
astrocyte-like tumor

Figure 3. SCRAM uncovers new tumour cell states and developmental hierarchies in glioma. (A) Dimplot and corresponding pie chart showing Single-Cell Rule Association Mining (SCRAM)-identified astrocyte-like tumour cells for Cluster 1 in human glioma samples. Copy-number variant (CNV)-harbouring cells are outlined in black. (B) Feature plots showing exemplary large-scale CNVs. (C) Density plots showing single-nucleotide variant (SNV) density. (D) Feature plots for select tumour cell (*CDK4, EGFR*) and astrocyte (*ALDH1L1, ALDOC, AQP4, GFAP, S100B, SLC1A3*) markers. (E) Co-occurring CNVs for five patient-matched *IDH1*–wild-type ($IDH1^{WT}$) glioma samples show leading edge cells emanate from specific co-occurring CNV lineages. Increased line thickness (weight) indicates more frequent co-occurrence. (F) RNA velocity lineage tracing by SCRAM-assigned cell type shows astrocyte-like tumour cells derive from stem-like and progenitor-like tumour cells and transition through an intermediate cell state marked by embryonic astrocytic and radial glial signatures. (G) RNA velocity pseudotime plots. (H) RNA velocity lineage tracing by tumour sample location shows leading edge cells are derived from glioma cells in the tumour core. (I) Dimplot and corresponding pie chart showing SCRAM-identified stem-like and progenitor-like cell type annotations for Cluster 23 cells in human glioma samples. CNV-harbouring cells are outlined in black. (J) Feature plots showing exemplary large-scale CNVs. (K) Density plot showing SNV density. (L) Feature plots for select embryonic astrocyte (*LGALS3, TIMP1*), GSC (*CCND2, OLIG2, SOX2*), LEC (*PDPN, PROX1*), NSC (*HES1, NES, SOX2, SOX9*), RG *(CDH2, HES1, NES, SOX2, TNC*) and oligodendrocyte (*OLIG2*) markers. (M) Schematic showing astrocyte-like tumour cells with multiple co-occurring CNVs in the leading edge emerge from embryonic astrocyte-like tumour cells with similar CNV profiles. Embryonic astrocyte-like tumour cells derive from stem-like and progenitor-like tumour cells in the core and feature single CNVs. GSC: glioma stem cell; LEC: lymphatic endothelial cell; NSC: neural stem cell; RG: radial glia.

488 **Figure 4**

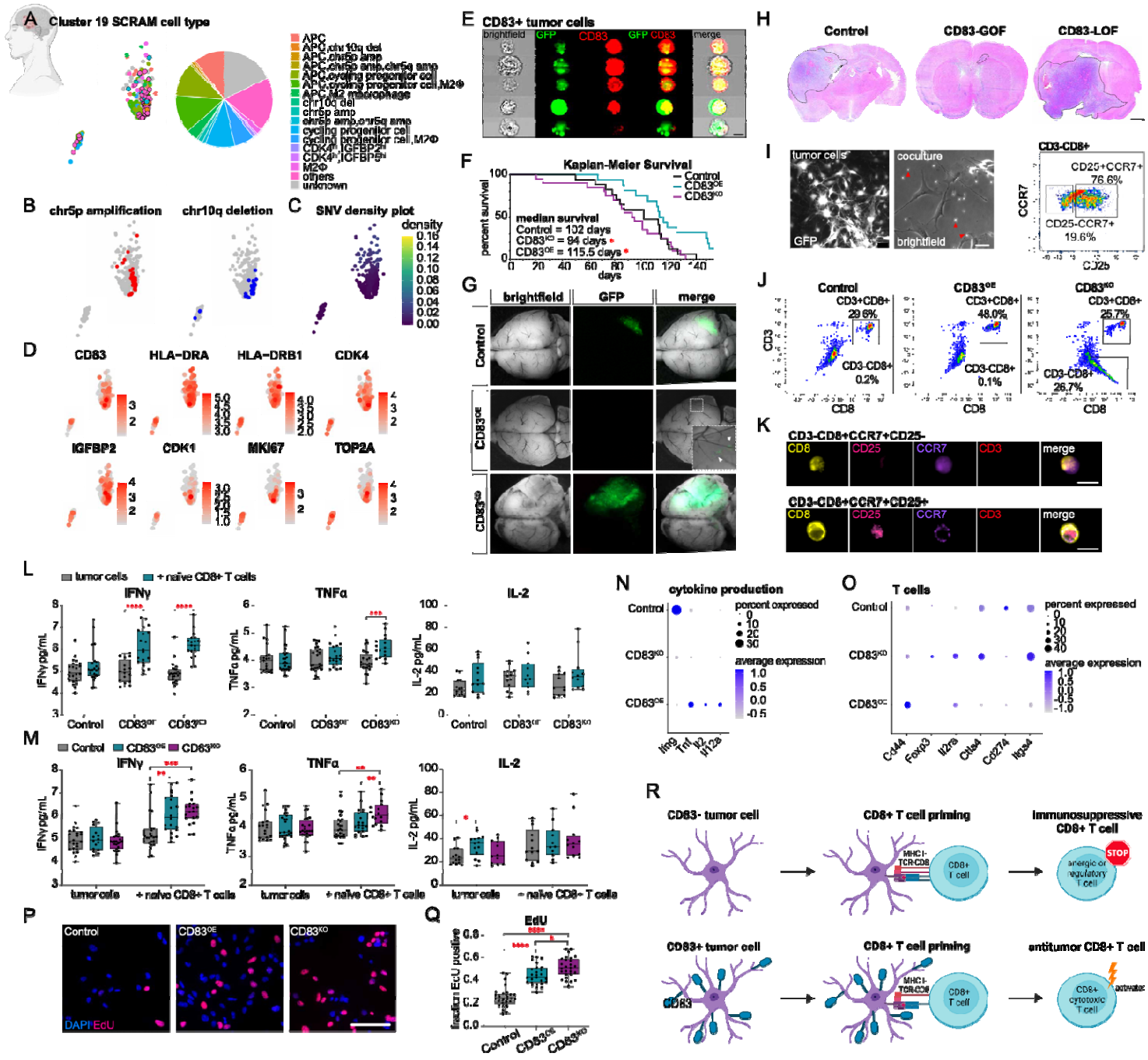
A
Cluster 19 SCRAM cell type
APC
APC,chr10q del
APC,chr5p amp
APC,chr5p amp,chr5q amp
APC,cycling progenitor cell
APC,cycling progenitor cell,M2Φ
APC,M2 macrophage
chr10q del
chr5p amp
chr5p amp,chr5q amp
cycling progenitor cell
cycling progenitor cell,M2Φ
CDK4Φ,IGFBP2hi
CDK4hi,IGFBP5hi
M2Φ
others
unknown
B
chr5p amplification
chr10q deletion
C
SNV density plot
density
D
CD83
HLA-DRA
HLA-DRB1
CDK4
IGFBP2
CDK1
MKI67
TOP2A
E
CD83+ tumor cells
brightfield
GFP
CD83
GFP CD83
merge
F
Kaplan-Meier Survival
percent survival
days
Control
CD83OE
CD83KO
median survival
Control = 102 days
CD83KO = 94 days
CD83OE = 115.5 days
G
brightfield
GFP
merge
Control
CD83OE
CD83KO
H
Control
CD83-GOF
CD83-LOF
I
tumor cells
coculture
GFP
brightfield
CD3-CD8+
CD25+CCR7+
76.6%
CD25-CCR7+
19.6%
CCR7
CD25
J
Control
CD83OE
CD83KO
CD3+CD8+
29.6%
48.0%
25.7%
CD3-CD8+
0.2%
0.1%
26.7%
CD3
CD8
K
CD3-CD8+CCR7+CD25-
CD8
CD25
CCR7
CD3
merge
CD3-CD8+CCR7+CD25+
L
tumor cells
+ naive CD8+ T cells
IFNγ
TNFα
IL-2
IFNγ pg/mL
TNFα pg/mL
IL-2 pg/mL
Control
CD83OE
CD83KO
M
Control
CD83OE
CD83KO
IFNγ
TNFα
IL-2
tumor cells
+ naive CD8+ T cells
N
cytokine production
Control
CD83KO
CD83OE
percent expressed
average expression
Ifng
Tnf
Il2
Il12a
O
T cells
Control
CD83KO
CD83OE
percent expressed
average expression
Cd44
Foxp3
Il2ra
Ctla4
Cd274
Itga4
R
CD83- tumor cell
CD8+ T cell priming
Immunosuppressive CD8+ T cell
MHCI-TCR-CD8
CD8+ T cell
STOP
anergic or regulatory T cell
CD83+ tumor cell
CD8+ T cell priming
antitumor CD8+ T cell
CD83
MHCI-TCR-CD8
CD8+ T cell
CD8+ cytotoxic T cell
activator
P
Control
CD83OE
CD83KO
DAPI EdU
Q
EdU
fraction EdU positive
Control
CD83OE
CD83KO

Figure 4. SCRAM-identified APC-like tumour cells mediate disease progression by restricting the immunosuppressive landscape in glioma. (A) Dimplot and corresponding pie chart showing Single-Cell Rule Association Mining (SCRAM)-identified antigen-presenting cell (APC)-like tumour cells (ALTs) for Cluster 19 in human glioma samples. Copy-number variant (CNV)-harbouring cells are outlined in black. (B) Feature plots showing exemplary large-scale CNVs. (C) Density plots showing single-nucleotide variant (SNV) density. (D) Feature plots for select tumour cell (*CDK4, IGFBP2*), cycling progenitor cell (*CDK1, CENPF, MKI67, TOP2A*), and APC (*CD83, HLA-DRA, HLA-DRB1*) markers. (E) Representative images from imaging flow cytometry of $CD83^{+}GFP^{+}$ ALTs demonstrating diffuse GFP expression throughout the cell; scale bar: 7 µm. (F) Kaplan–Meier survival analysis of mice bearing control (n=17), CD83 overexpressing ($CD83^{OE}$; n=16), and CD83 knockout ($CD83^{KO}$; n=20) tumours; $*p<0.05$. (G) Exemplary brightfield and GFP images from age-matched control, $CD83^{OE}$, and $CD83^{KO}$ tumours. (H) Representative haematoxylin and eosin whole-brain coronal sections from age-matched control, $CD83^{OE}$, and $CD83^{KO}$ tumours; black dotted lines denote tumour regions, scale bar: 1 mm. (I) Representative images from cell lines established from age-matched control, $CD83^{OE}$, and $CD83^{KO}$ tumours; scale bar: 20 µm. (J) Imaging flow cytometry plots showing an increased percentage of $CD3^{+}CD8^{-}$ T cells from $CD83^{OE}$ (48.0%) co-cultures compared with controls (29.6%) and $CD83^{KO}$ (25.7%) co-cultures. $CD3^{-}CD8^{+}$ T cells detected in 26.7% of $CD83^{KO}$ T cells compared with 0.2% in control and 0.1% in $CD83^{OE}$ T cells. Gating on $CD3^{-}CD8^{+}$ T cells from $CD83^{KO}$ co-cultures shows two T cell populations: $CD3^{-}CD8^{+}CCR7^{+}CD25^{-}$ T cells (19.6%) and $CD3^{-}CD8^{+}CCR7^{+}CD25^{+}$ T cells (76.6%). (K) Representative images of $CD3^{-}CD8^{+}CCR7^{+}CD25^{-}$ and $CD3^{-}CD8^{+}CCR7^{+}CD25^{+}$ T cells from co-culture imaging flow cytometry experiments; scale bar: 7 µm. (L) Box and whisker plots for enzyme-linked immunosorbent assays (ELISA) show increased interferon-gamma (IFNγ) production in $CD83^{OE}$ ($****p<0.0001$) and $CD83^{KO}$ ($****p<0.0001$) co-cultures containing naïve $CD8^{+}$ T cells. Tumour necrosis factor-alpha (TNFα) production only increased in $CD83^{KO}$ co-

cultures (***p<0.001); interleukin (IL)-2 production was unchanged. (M) Box and whisker plots for ELISAs show IFNγ production is increased in CD83^{OE} (**p<0.01) and CD83^{KO} (****p<0.001) T cell co-cultures relative to control co-cultures (***p<0.001). TNFα production increased in CD83^{KO} T cell co-cultures compared with CD83^{OE} (**p<0.01) and control cl-cultures (**p<0.01). IL-2 production increased in CD83^{OE} cells cultured in the absence of T cells compared with controls (*p<0.05). (N) Dot plots from control, CD83^{OE}, and CD83^{KO} tumour single-cell RNA-sequencing (scRNA-seq) datasets show *in vivo* T cells enriched for *Ifng* (IFNγ) expression in control tumours and *Tnf* (TNFα), *Il2* (IL-2), and *Il12a* (IL-12) in CD83^{OE} tumours. (O) Dot plots from control, CD83^{OE}, and CD83^{KO} tumour scRNA-seq datasets show T cells enriched for effector and memory T cell markers (*Cd44, Il2ra*) in CD83^{OE} tumours and anergic and regulatory T cell markers (*Foxp3, Il2ra, Ctla4, Itga4*) in CD83^{KO} tumours. (P) Representative images from EdU proliferation assays on control, CD83^{OE}, and CD83^{KO} tumour cell lines *in vitro*. (U) Quantification of EdU+ cells for CD83^{OE} (****p<0.0001) and CD83^{KO} (****p<0.0001) cells, which are more proliferative than control cells; CD83^{KO} cells are more proliferative than CD83^{OE} cells (*p<0.05). (P) Schematic showing CD83 expression in tumour cells enables CD8^{+} T cell activation, whereas CD83 loss promotes immunosuppressive T cell phenotypes.

531 **Figure 5**

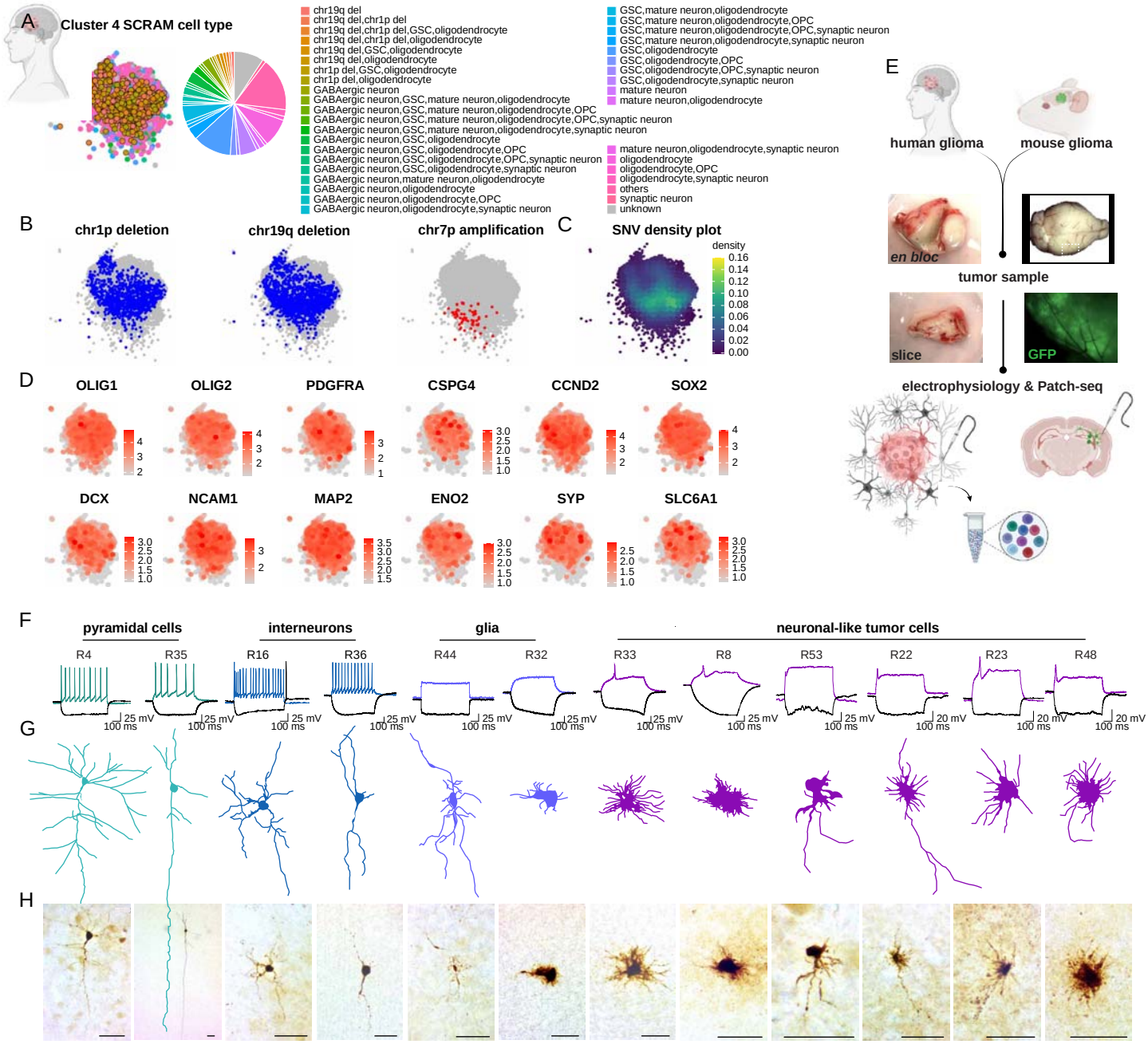
A
Cluster 4 SCRAM cell type
chr19q del
chr19q del,chr1p del
chr19q del,chr1p del,GSC,oligodendrocyte
chr19q del,chr1p del,oligodendrocyte
chr19q del,GSC,oligodendrocyte
chr19q del,oligodendrocyte
chr1p del,GSC,oligodendrocyte
chr1p del,oligodendrocyte
GABAergic neuron
GABAergic neuron,GSC,mature neuron,oligodendrocyte
GABAergic neuron,GSC,mature neuron,oligodendrocyte,OPC
GABAergic neuron,GSC,mature neuron,oligodendrocyte,OPC,synaptic neuron
GABAergic neuron,GSC,mature neuron,oligodendrocyte,synaptic neuron
GABAergic neuron,GSC,oligodendrocyte
GABAergic neuron,GSC,oligodendrocyte,OPC
GABAergic neuron,GSC,oligodendrocyte,OPC,synaptic neuron
GABAergic neuron,GSC,oligodendrocyte,synaptic neuron
GABAergic neuron,mature neuron,oligodendrocyte
GABAergic neuron,oligodendrocyte
GABAergic neuron,oligodendrocyte,OPC
GABAergic neuron,oligodendrocyte,synaptic neuron
GSC,mature neuron,oligodendrocyte
GSC,mature neuron,oligodendrocyte,OPC
GSC,mature neuron,oligodendrocyte,OPC,synaptic neuron
GSC,mature neuron,oligodendrocyte,synaptic neuron
GSC,oligodendrocyte
GSC,oligodendrocyte,OPC
GSC,oligodendrocyte,OPC,synaptic neuron
GSC,oligodendrocyte,synaptic neuron
mature neuron
mature neuron,oligodendrocyte
mature neuron,oligodendrocyte,synaptic neuron
oligodendrocyte
oligodendrocyte,OPC
oligodendrocyte,synaptic neuron
others
synaptic neuron
unknown
B
chr1p deletion
chr19q deletion
chr7p amplification
C
SNV density plot
density
0.16
0.14
0.12
0.10
0.08
0.06
0.04
0.02
0.00
D
OLIG1
OLIG2
PDGFRA
CSPG4
CCND2
SOX2
DCX
NCAM1
MAP2
ENO2
SYP
SLC6A1
E
human glioma
mouse glioma
en bloc
tumor sample
slice
GFP
electrophysiology & Patch-seq
F
pyramidal cells
interneurons
glia
neuronal-like tumor cells
R4
R35
R16
R36
R44
R32
R33
R8
R53
R22
R23
R48
25 mV
20 mV
100 ms
G
H

Figure 5. Neuron-like tumour cells are specific to *IDH1*-mutant glioma and functionally similar to neurons. (A) Dimplot and corresponding pie chart showing Single-Cell Rule Association Mining (SCRAM)-identified neuron-like tumour cells (NLTs) for Cluster 4 in human glioma samples. Copy-number variant (CNV)-harbouring cells are outlined in black. (B) Feature plots showing exemplary large-scale CNVs. (C) Density plot showing single-nucleotide variant (SNV) density. (D) Feature plots for select GSC (*CCND2, OLIG2, SOX2*), oligodendrocyte (*OLIG1, OLIG2*), OPC (*PDGFRA, CSPG4*), mature neuron (*MAP2, ENO2*), synaptic neuron *(MAP2, ENO2, SYP*), and GABAergic neuron (*DCX, NCAM1, SLC6A1*) markers. (E) Experimental workflow for whole-cell recordings and whole-cell patch clamp recordings, followed by singe-cell RNA-sequencing (Patch-seq) assays. (F) Exemplary membrane responses from patched *IDH1*-mutant ($IDH1^{mut}$) cells to a 600-ms hyperpolarizing current step (black) and suprathreshold depolarizing current step (coloured). Two voltage traces are shown: the hyperpolarization trace obtained with injected currents (black) and the depolarization trace showing maximal AP firing rate; injected current: −100 pA. (G) Matched traced cell morphologies are shown for recorded cells. (H) Matched images of biocytin-filled cell morphologies for patched cells; scale bar: 50 µm. AP: action potential; GABA: γ-aminobutyric acid; GSC: glioma stem cell; OPC: oligodendrocyte precursor cell.

Figure 6

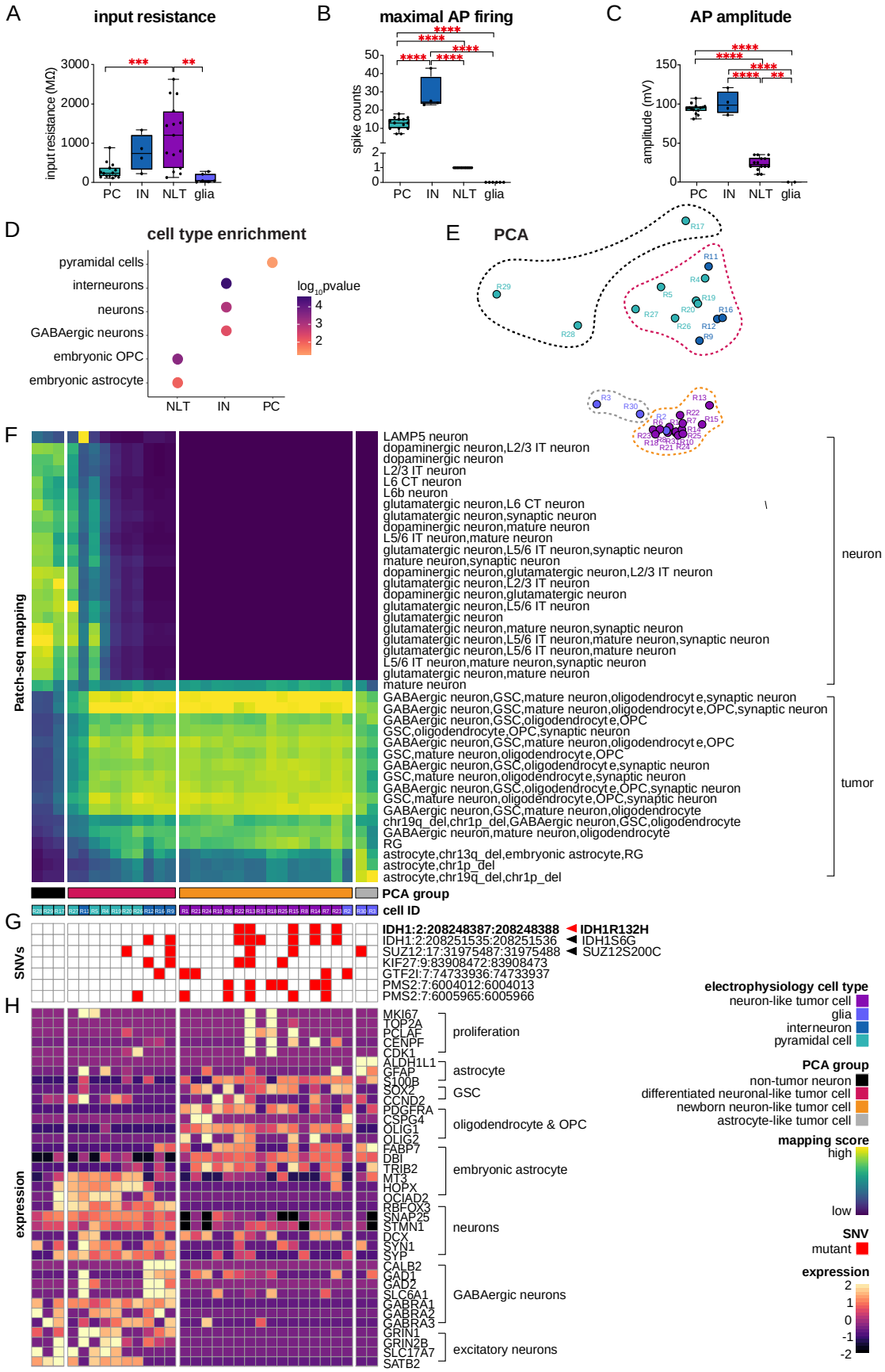
A
input resistance
input resistance (MΩ)
3000
2000
1000
0
***
**
PC
IN
NLT
glia
B
maximal AP firing
spike counts
50
40
30
20
10
2
1
0
****
PC
IN
NLT
glia
C
AP amplitude
amplitude (mV)
150
100
50
0
****
**
PC
IN
NLT
glia
D
cell type enrichment
pyramidal cells
interneurons
neurons
GABAergic neurons
embryonic OPC
embryonic astrocyte
NLT
IN
PC
log10pvalue
4
3
2
E
PCA
F
Patch-seq mapping
LAMP5 neuron
dopaminergic neuron,L2/3 IT neuron
dopaminergic neuron
L2/3 IT neuron
L6 CT neuron
L6b neuron
glutamatergic neuron,L6 CT neuron
glutamatergic neuron,synaptic neuron
dopaminergic neuron,mature neuron
L5/6 IT neuron,mature neuron
glutamatergic neuron,L5/6 IT neuron,synaptic neuron
mature neuron,synaptic neuron
dopaminergic neuron,glutamatergic neuron,L2/3 IT neuron
glutamatergic neuron,L2/3 IT neuron
dopaminergic neuron,glutamatergic neuron
glutamatergic neuron,L5/6 IT neuron
glutamatergic neuron
glutamatergic neuron,mature neuron,synaptic neuron
glutamatergic neuron,L5/6 IT neuron,mature neuron,synaptic neuron
glutamatergic neuron,L5/6 IT neuron,mature neuron
L5/6 IT neuron,mature neuron,synaptic neuron
glutamatergic neuron,mature neuron
mature neuron
GABAergic neuron,GSC,mature neuron,oligodendrocyte,synaptic neuron
GABAergic neuron,GSC,mature neuron,oligodendrocyte,OPC,synaptic neuron
GABAergic neuron,GSC,oligodendrocyte,OPC
GSC,oligodendrocyte,OPC,synaptic neuron
GABAergic neuron,GSC,mature neuron,oligodendrocyte,OPC
GSC,mature neuron,oligodendrocyte,OPC
GABAergic neuron,GSC,oligodendrocyte,synaptic neuron
GSC,mature neuron,oligodendrocyte,synaptic neuron
GABAergic neuron,GSC,oligodendrocyte,OPC,synaptic neuron
GSC,mature neuron,oligodendrocyte,OPC,synaptic neuron
GABAergic neuron,GSC,mature neuron,oligodendrocyte
chr19q_del,chr1p_del,GABAergic neuron,GSC,oligodendrocyte
GABAergic neuron,mature neuron,oligodendrocyte
RG
astrocyte,chr13q_del,embryonic astrocyte,RG
astrocyte,chr1p_del
astrocyte,chr19q_del,chr1p_del
neuron
tumor
PCA group
cell ID
G
SNVs
IDH1:2:208248387:208248388
IDH1R132H
IDH1:2:208251535:208251536
IDH1S6G
SUZ12:17:31975487:31975488
SUZ12S200C
KIF27:9:83908472:83908473
GTF2I:7:74733936:74733937
PMS2:7:6004012:6004013
PMS2:7:6005965:6005966
H
expression
MKI67
TOP2A
PCLAF
CENPF
CDK1
proliferation
ALDH1L1
GFAP
astrocyte
S100B
SOX2
CCND2
GSC
PDGFRA
CSPG4
OLIG1
OLIG2
oligodendrocyte & OPC
FABP7
DBI
TRIB2
MT3
HOPX
OCIAD2
embryonic astrocyte
RBFOX3
SNAP25
STMN1
DCX
SYN1
SYP
neurons
CALB2
GAD1
GAD2
SLC6A1
GABRA1
GABRA2
GABRA3
GABAergic neurons
GRIN1
GRIN2B
SLC17A7
SATB2
excitatory neurons
electrophysiology cell type
neuron-like tumor cell
glia
interneuron
pyramidal cell
PCA group
non-tumor neuron
differentiated neuronal-like tumor cell
newborn neuron-like tumor cell
astrocyte-like tumor cell
mapping score
high
low
SNV
mutant
expression
2
1
0
-1
-2

Figure 6. Neuron-like tumour cells are a novel cell type with unique electrophysiological, transcriptomic and genomic profiles. (A) Bar graph showing neuron-like tumour cells (NLTs) have higher input resistance compared with non-tumour neurons; *p*-values for pairwise comparisons are noted in the figure. PC: pyramidal cell; IN: interneuron. (B) Bar graph showing NLTs fire fewer spikes compared to neurons; *p*-values for pairwise comparisons are noted in the figure. (C) Bar graph showing NLTs have smaller action potential (AP) amplitudes compared to neurons; *p*-values for pairwise comparisons are noted in the figure. (D) EnrichR analysis of 31 cells analysed by whole-cell patch clamp recordings, followed by single-cell RNA-sequencing (Patch-seq), confirms NLTs are enriched for gene sets corresponding to oligodendrocyte precursor cells (OPCs) and embryonic astrocytes; $p<0.05$. (E) Principal component analysis (PCA) plot of 31 Patch-seq cells shows clustering of cells based on electrophysiological properties. Newborn NLTs are transcriptionally similar to each other and glia, whereas differentiated NLTs resemble non-tumour pyramidal cells. Cells are coloured according to electrophysiological properties; dotted lines show PCA groups. (F) Mapping Patch-seq cells to Single-Cell Rule Association Mining (SCRAM)-annotated single-cell RNA-sequencing human glioma dataset and (G) single-nucleotide variant (SNV) analysis shows newborn NLTs map strongly to NLT annotations, whereas differentiated NLTs map to both non-tumour neurons and NLTs. Astrocyte-like tumour cells show reduced NLT profiles and map most strongly to astrocyte-like, chromosome 1p19q co-deleted tumour cells from *IDH1*-mutant ($IDH1^{mut}$) oligodendroglioma. (G) The top seven most frequently occurring SNVs are shown for each cell. (H) Heatmap showing expression of representative genes from neural, glioma, and proliferating cell types. Proliferation markers are only detected in newborn and differentiated NLTs. GSC: glioma stem cell; RG: radial glia.

References

1. Kolodziejczyk, A. A., Kim, J. K., Svensson, V., Marioni, J. C. & Teichmann, S. A. The technology and biology of single-cell RNA sequencing. *Mol. Cell* **58**, 610–620 (2015).
2. Couturier, C. P. *et al.* Single-cell RNA-seq reveals that glioblastoma recapitulates a normal neurodevelopmental hierarchy. *Nature Communications* vol. 11 Preprint at https://doi.org/10.1038/s41467-020-17186-5 (2020).
3. Tirosh, I. *et al.* Single-cell RNA-seq supports a developmental hierarchy in human oligodendroglioma. *Nature* **539**, 309–313 (2016).
4. Patel, A. P. *et al.* Single-cell RNA-seq highlights intratumoral heterogeneity in primary glioblastoma. *Science* **344**, 1396–1401 (2014).
5. Neftel, C. *et al.* An Integrative Model of Cellular States, Plasticity, and Genetics for Glioblastoma. *Cell* **178**, 835-849.e21 (2019).
6. Kuleshov, M. V. *et al.* Enrichr: a comprehensive gene set enrichment analysis web server 2016 update. *Nucleic Acids Res.* **44**, W90-7 (2016).
7. Tasic, B. *et al.* Shared and distinct transcriptomic cell types across neocortical areas. *Nature* **563**, 72–78 (2018).
8. Hodge, R. D. *et al.* Conserved cell types with divergent features in human versus mouse cortex. *Nature* **573**, 61–68 (2019).
9. Richards, L. M. *et al.* Gradient of Developmental and Injury Response transcriptional states defines functional vulnerabilities underpinning glioblastoma heterogeneity. *Nat Cancer* **2**, 157–173 (2021).
10. Harmanci, A. S., Harmanci, A. O. & Zhou, X. CaSpER identifies and visualizes CNV events by integrative analysis of single-cell or bulk RNA-sequencing data. *Nature Communications* vol. 11 Preprint at https://doi.org/10.1038/s41467-019-13779-x (2020).
11. Harmanci, A. O., Harmanci, A. S., Klisch, T. & Patel, A. J. XCVATR: Characterization of Variant Impact on the Embeddings of Single -Cell and Bulk RNA-Sequencing Samples. Preprint at https://doi.org/10.1101/2021.06.01.446668.

12. Bai, H. *et al.* Integrated genomic characterization of IDH1-mutant glioma malignant progression. *Nat. Genet.* **48**, 59–66 (2016).
13. Harmancı, A. S. *et al.* Integrated genomic analyses of de novo pathways underlying atypical meningiomas. *Nat. Commun.* **9**, 16215 (2018).
14. Zhang, M. *et al.* Somatic mutations of SUZ12 in malignant peripheral nerve sheath tumors. *Nat. Genet.* **46**, 1170–1172 (2014).
15. Lee, W. *et al.* PRC2 is recurrently inactivated through EED or SUZ12 loss in malignant peripheral nerve sheath tumors. *Nat. Genet.* **46**, 1227–1232 (2014).
16. Sottoriva, A. *et al.* Intratumor heterogeneity in human glioblastoma reflects cancer evolutionary dynamics. *Proc. Natl. Acad. Sci. U. S. A.* **110**, 4009–4014 (2013).
17. Bergen, V., Lange, M., Peidli, S., Wolf, F. A. & Theis, F. J. Generalizing RNA velocity to transient cell states through dynamical modeling. *Nat. Biotechnol.* **38**, 1408–1414 (2020).
18. Fujimoto, Y. *et al.* CD83 expression influences CD4+ T cell development in the thymus. *Cell* **108**, 755–767 (2002).
19. Neefjes, J., Jongsma, M. L. M., Paul, P. & Bakke, O. Towards a systems understanding of MHC class I and MHC class II antigen presentation. *Nat. Rev. Immunol.* **11**, 823–836 (2011).
20. Lecoultre, M., Dutoit, V. & Walker, P. R. Phagocytic function of tumor-associated macrophages as a key determinant of tumor progression control: a review. *J. Immunother. Cancer* **8**, (2020).
21. Park, Y. *et al.* Imaging flow cytometry protocols for examining phagocytosis of microplastics and bioparticles by immune cells of aquatic animals. *Front. Immunol.* **11**, 203 (2020).
22. Chen, F. & LoTurco, J. A method for stable transgenesis of radial glia lineage in rat neocortex by piggyBac mediated transposition. *J. Neurosci. Methods* **207**, 172–180 (2012).
23. Breloer, M. & Fleischer, B. CD83 regulates lymphocyte maturation, activation and homeostasis. *Trends Immunol.* **29**, 186–194 (2008).

24. Irving, B. A. & Weiss, A. The cytoplasmic domain of the T cell receptor zeta chain is sufficient to couple to receptor-associated signal transduction pathways. *Cell* **64**, 891–901 (1991).
25. Baniyash, M. TCR zeta-chain downregulation: curtailing an excessive inflammatory immune response. *Nat. Rev. Immunol.* **4**, 675–687 (2004).
26. Farber, D. L., Yudanin, N. A. & Restifo, N. P. Human memory T cells: generation, compartmentalization and homeostasis. *Nat. Rev. Immunol.* **14**, 24–35 (2014).
27. Ziegler, E. *et al.* CCR7 signaling inhibits T cell proliferation. *J. Immunol.* **179**, 6485–6493 (2007).
28. Suzuki, M. *et al.* CD8+CD45RA+CCR7+FOXP3+ T cells with immunosuppressive properties: a novel subset of inducible human regulatory T cells. *J. Immunol.* **189**, 2118–2130 (2012).
29. Bradley, J. R. TNF-mediated inflammatory disease. *J. Pathol.* **214**, 149–160 (2008).
30. Siegel, J. P. Effects of interferon-gamma on the activation of human T lymphocytes. *Cell. Immunol.* **111**, 461–472 (1988).
31. Blachère, N. E. *et al.* IL-2 is required for the activation of memory CD8+ T cells via antigen cross-presentation. *J. Immunol.* **176**, 7288–7300 (2006).
32. Dutt, S. *et al.* CD8+CD44(hi) but not CD4+CD44(hi) memory T cells mediate potent graft antilymphoma activity without GVHD. *Blood* **117**, 3230–3239 (2011).
33. Jiang, X. *et al.* Principles of connectivity among morphologically defined cell types in adult neocortex. *Science* **350**, aac9462 (2015).
34. Scala, F. *et al.* Phenotypic variation of transcriptomic cell types in mouse motor cortex. *Nature* **598**, 144–150 (2021).
35. Drew, L. J., Fusi, S. & Hen, R. Adult neurogenesis in the mammalian hippocampus: why the dentate gyrus? *Learn. Mem.* **20**, 710–729 (2013).

36. Espósito, M. S. *et al.* Neuronal differentiation in the adult hippocampus recapitulates embryonic development. *J. Neurosci.* **25**, 10074–10086 (2005).

37. Overstreet Wadiche, L., Bromberg, D. A., Bensen, A. L. & Westbrook, G. L. GABAergic signaling to newborn neurons in dentate gyrus. *J. Neurophysiol.* **94**, 4528–4532 (2005).

38. Xie, Z. *et al.* Gene set knowledge discovery with Enrichr. *Curr Protoc* **1**, e90 (2021).

39. Winter, A. G. *et al.* RNA polymerase III transcription factor TFIIIC2 is overexpressed in ovarian tumors. *Proc. Natl. Acad. Sci. U. S. A.* **97**, 12619–12624 (2000).

40. White, R. J. RNA polymerase III transcription and cancer. *Oncogene* **23**, 3208–3216 (2004).

41. Saracci, R., IARC & Wild, C. P. *International Agency for Research on Cancer*. (IARC, 2015).

42. Habashy, K. J., Mansour, R., Moussalem, C., Sawaya, R. & Massaad, M. J. Challenges in glioblastoma immunotherapy: mechanisms of resistance and therapeutic approaches to overcome them. *Br. J. Cancer* **127**, 976–987 (2022).

43. Buerki, R. A., Chheda, Z. S. & Okada, H. Immunotherapy of primary brain tumors: Facts and hopes. *Clin. Cancer Res.* **24**, 5198–5205 (2018).

44. Grabowski, M. M. *et al.* Immune suppression in gliomas. *J. Neurooncol.* **151**, 3–12 (2021).

45. Woroniecka, K. I., Rhodin, K. E., Chongsathidkiet, P., Keith, K. A. & Fecci, P. E. T-cell dysfunction in glioblastoma: Applying a new framework. *Clin. Cancer Res.* **24**, 3792–3802 (2018).

46. Cornel, A. M., Mimpen, I. L. & Nierkens, S. MHC class I downregulation in cancer: Underlying mechanisms and potential targets for cancer immunotherapy. *Cancers (Basel)* **12**, 1760 (2020).

47. Zagzag, D. *et al.* Downregulation of major histocompatibility complex antigens in invading glioma cells: stealth invasion of the brain. *Lab. Invest.* **85**, 328–341 (2005).

48. de Charette, M., Marabelle, A. & Houot, R. Turning tumour cells into antigen presenting cells: The next step to improve cancer immunotherapy? *Eur. J. Cancer* **68**, 134–147 (2016).

49. Yu, J. S. *et al.* Vaccination with tumor lysate-pulsed dendritic cells elicits antigen-specific, cytotoxic T-cells in patients with malignant glioma. *Cancer Res.* **64**, 4973–4979 (2004).

50. Bu, N. *et al.* Exosome-loaded dendritic cells elicit tumor-specific CD8+ cytotoxic T cells in patients with glioma. *J. Neurooncol.* **104**, 659–667 (2011).

51. Tze, L. E. *et al.* CD83 increases MHC II and CD86 on dendritic cells by opposing IL-10-driven MARCH1-mediated ubiquitination and degradation. *J. Exp. Med.* **208**, 149–165 (2011).

52. Liu, H. *et al.* Ubiquitin ligase MARCH 8 cooperates with CD83 to control surface MHC II expression in thymic epithelium and CD4 T cell selection. *J. Exp. Med.* **213**, 1695–1703 (2016).

53. Yu, K. *et al.* PIK3CA variants selectively initiate brain hyperactivity during gliomagenesis. *Nature* **578**, 166–171 (2020).

54. John Lin, C.-C. *et al.* Identification of diverse astrocyte populations and their malignant analogs. *Nat. Neurosci.* **20**, 396–405 (2017).

55. Venkatesh, H. S. *et al.* Electrical and synaptic integration of glioma into neural circuits. *Nature* **573**, 539–545 (2019).

56. Venkataramani, V. *et al.* Glutamatergic synaptic input to glioma cells drives brain tumour progression. *Nature* **573**, 532–538 (2019).

57. Barron, T. *et al.* GABAergic neuron-to-glioma synapses in diffuse midline gliomas. (2022) doi:10.1101/2022.11.08.515720.

58. Correia, C. E., Umemura, Y., Flynn, J. R., Reiner, A. S. & Avila, E. K. Pharmacoresistant seizures and IDH mutation in low-grade gliomas. *Neurooncol Adv* **3**, vdab146 (2021).

59. Shoshan, Y. *et al.* Expression of oligodendrocyte progenitor cell antigens by gliomas: implications for the histogenesis of brain tumors. *Proc. Natl. Acad. Sci. U. S. A.* **96**, 10361–10366 (1999).

60. Rebetz, J. *et al.* Glial progenitor-like phenotype in low-grade glioma and enhanced CD133-expression and neuronal lineage differentiation potential in high-grade glioma. *PLoS One* **3**, e1936 (2008).

61. Ledur, P. F. *et al.* Culture conditions tailored to the cell of origin are critical for maintaining native properties and tumorigenicity of glioma cells. *Neuro. Oncol.* **18**, 1413–1424 (2016).

62. Tate, J. G. *et al.* COSMIC: The Catalogue Of Somatic Mutations In Cancer. *Nucleic Acids Res.* **47**, D941–D947 (2019).

63. Sherry, S. T. *et al.* dbSNP: the NCBI database of genetic variation. *Nucleic Acids Res.* **29**, 308–311 (2001).

64. Scrucca, L., Fop, M., Murphy, T. B. & Raftery, A. E. Mclust 5: Clustering, classification and density estimation using Gaussian finite mixture models. *R J.* **8**, 289–317 (2016).

65. Korsunsky, I. *et al.* Fast, sensitive and accurate integration of single-cell data with Harmony. *Nat. Methods* **16**, 1289–1296 (2019).

66. Dobin, A. *et al.* STAR: ultrafast universal RNA-seq aligner. *Bioinformatics* **29**, 15–21 (2013).

67. Liao, Y., Smyth, G. K. & Shi, W. featureCounts: an efficient general purpose program for assigning sequence reads to genomic features. *Bioinformatics* **30**, 923–930 (2014).

68. Harrow, J. *et al.* GENCODE: The reference human genome annotation for The ENCODE Project. *Genome Res.* **22**, 1760–1774 (2012).

69. Love, M. I., Huber, W. & Anders, S. Moderated estimation of fold change and dispersion for RNA-seq data with DESeq2. *Genome Biol.* **15**, 550 (2014).

70. Ritchie, M. E. *et al.* limma powers differential expression analyses for RNA-sequencing and microarray studies. *Nucleic Acids Res.* **43**, e47 (2015).

71. Robinson, J. T. *et al.* Integrative genomics viewer. *Nat. Biotechnol.* **29**, 24–26 (2011).

72. Zhu, W. *et al.* Daam2 driven degradation of VHL promotes gliomagenesis. *Elife* **6**, (2017).

73. Cadwell, C. R. *et al.* Electrophysiological, transcriptomic and morphologic profiling of single neurons using Patch-seq. *Nat. Biotechnol.* **34**, 199–203 (2016).

74. Cadwell, C. R. *et al.* Multimodal profiling of single-cell morphology, electrophysiology, and gene expression using Patch-seq. *Nat. Protoc.* **12**, 2531–2553 (2017).

75. Picelli, S. *et al.* Full-length RNA-seq from single cells using Smart-seq2. *Nat. Protoc.* **9**, 171–181 (2014).

76. Aiba, I., West, A. K., Sheline, C. T. & Shuttleworth, C. W. Intracellular dialysis disrupts Zn2+ dynamics and enables selective detection of Zn2+ influx in brain slice preparations. *J. Neurochem.* **125**, 822–831 (2013).

77. Meyer, J., Yu, K., Deneen, B. & Noebels, J. Glioblastoma disrupts cortical network activity at multiple spatial and temporal scales. *bioRxiv* 2022.08.31.505988 (2022) doi:10.1101/2022.08.31.505988.

78. Friedrich, J., Zhou, P. & Paninski, L. Fast online deconvolution of calcium imaging data. *PLoS Comput. Biol.* **13**, e1005423 (2017).